ACS APPLIED MATERIALS & INTERFACES

Research Article

www.acsami.org

Superhydrophobic Hybrid Inorganic–Organic Thiol-ene Surfaces Fabricated via Spray-Deposition and Photopolymerization

Bradley J. Sparks, Ethan F. T. Hoff, Li Xiong, James T. Goetz, and Derek L. Patton*

School of Polymers and High Performance Materials, University of Southern Mississippi, 118 College Drive, Number 5050, Hattiesburg, Mississippi 39406, United States

Supporting Information

ABSTRACT: We report a simple and versatile method for the fabrication of superhydrophobic inorganic–organic thiol-ene coatings via sequential spray-deposition and photopolymerization under ambient conditions. The coatings are obtained by spray-deposition of UV-curable hybrid inorganic–organic thiol-ene resins consisting of pentaerythritol tetra(3-mercaptopropionate) (PETMP), triallyl isocyanurate (TTT), 2,4,6,8-tetramethyl-2,4,6,8-tetravinylcyclotetrasiloxane (TMTVSi), and hydrophobic fumed silica nanoparticles. The spray-deposition process and nanoparticle agglomeration/dispersion provide surfaces with hierarchical morphologies exhibiting both micro- and nanoscale roughness. The wetting behavior, dependent on the concentration of TMTVSi and hydrophobic silica nanoparticles, can be varied over a broad range to ultimately provide coatings with high static water contact angles (>150°), low contact angle hysteresis, and low roll off angles (<5°). The cross-linked thiol-ene coatings are solvent resistant, stable at low and high pH, and maintain superhydrophobic wetting behavior after extended exposure to elevated temperatures. We demonstrate the versatility of the spray-deposition and UV-cure process on a variety of substrate surfaces including glass, paper, stone, and cotton fabric.

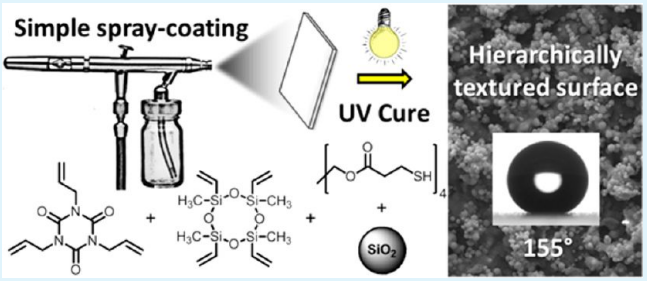

KEYWORDS: *superhydrophobic, thiol-ene, photopolymerization, spray-deposition, water repellent*

INTRODUCTION

Superhydrophobic surfaces exhibiting an apparent water contact angle of greater than 150° and low contact angle hysteresis have attracted a tremendous amount of attention due to potential applications in self-cleaning coatings, drag reduction, corrosion resistance, and high performance textiles.[1,2] It is well established that the superhydrophobic wetting state can be attributed to both chemical composition and geometric parameters (i.e., roughness) of the solid interface.[3] Specifically, the superhydrophobic wetting state is typically manifested on surfaces exhibiting a combination of low surface energy and an appropriately designed hierarchically structured surface comprised of dual-scale textures (typically nanometer scale features superimposed on underlying micrometer scale features). In general, the dual-scale surface roughness serves to either increase or decrease the contact area of the solid–liquid interface resulting in a so-called apparent contact angle. Either the liquid completely conforms to the surface roughness to increase the solid–liquid contact area, an adhesive wetting behavior described as the Wenzel[4] wetting state, or the liquid bridges between surface roughness protrusions creating a composite solid–liquid–air interface, a wetting behavior denoted as the Cassie–Baxter[5] wetting state. The composite interface associated with the Cassie–Baxter wetting state typically leads to high contact angles, low roll off angles, and correspondingly low contact angle hysteresis as exemplified by the lotus leaf (i.e., the lotus effect[6]).

Numerous physical and chemical approaches have been reported for the design of hierarchically structured surfaces from low surface energy materials in pursuit of the desirable Cassie–Baxter wetting state, including lithography,[7−9] self-assembly,[10] electrospinning,[11−14] chemical vapor deposition,[15−18] plasma or chemical etching,[19,20] and sol–gel techniques[21−23] among many others.[24,25] However, approaches capable of producing robust superhydrophobic surfaces using simple, low-cost, and industrially scalable techniques, parameters critical for practical applications, are rarely achieved. In this regard, many of the aforementioned approaches require multiple processing steps, expensive building blocks or equipment, and exhibit limitations in terms of substrate size and materials, all of which limit their practical applications. In contrast, spray-deposition provides a simple, one-step industrially viable process with a long history in coatings technology. Given such advantages, the spray-deposition process has recently been applied for the deposition of nanoparticle suspensions,[26,27] polymer/nanoparticle blends,[28−33] sol–gel precursors,[34] and copolymers[35−37] toward the fabrication of

Received: December 19, 2012
Accepted: February 14, 2013
Published: February 14, 2013

superhydrophobic surfaces on substrates of various shapes and compositions. Exceedingly few of the spray-deposition approaches reported to date, particularly those involving polymeric binders or matrix materials, have explored stabilization mechanisms (i.e., cross-linking) as a route to improve the chemical, mechanical, and thermal robustness of superhydrophobic surfaces.[32,38] Improvements to these robustness or durability factors are vital for widespread use of superhydrophobic materials.[39] In a recent example, Raza et al.[32] reported facile fabrication of superhydrophobic surfaces via spray deposition of a fluorinated benzoxazine monomer/silica nanoparticle solution onto glass followed by thermal polymerization yielding a cross-linked polybenzoxazine matrix. Although the films exhibited enhanced durability, high temperatures (220 °C) were required in the cure processing step, which may limit the utility of the approach on certain substrate materials. It should also be noted that outside of spray-deposition of superhydrophobic materials, there have been a number of excellent approaches that target improvements in mechanical deformation (i.e., abrasion, peeling, stretching, etc.),[38−43] temperature stability,[32] and solvent resistance[44] of nonwetting surfaces.

Herein, we report a simple and convenient method for the fabrication of robust superhydrophobic surfaces via sequential spray-deposition and thiol-ene photopolymerization. In addition to the salient features of spray-deposition, photopolymerization offers advantages such as rapid through-cure, ambient temperature processing, and spatial and temporal control over the polymerization.[45] Additionally, the free-radical step-growth thiol-ene process facilitated by a rapid, highly efficient chain transfer reaction between multifunctional alkenes and thiols provides insensitivity to oxygen inhibition enabling ambient atmosphere photopolymerization.[46,47] Superhydrophobic coatings are obtained by spray-deposition of UV-curable hybrid inorganic−organic thiol-ene resins consisting of pentaerythritol tetra(3-mercaptopropionate) (PETMP), triallyl isocyanurate (TTT), 2,4,6,8-tetramethyl-2,4,6,8-tetravinylcyclotetrasiloxane (TMTVSi), and hydrophobic fumed silica nanoparticles. The spray-deposition process and nanoparticle agglomeration/dispersion provide surfaces with hierarchical morphologies exhibiting both micro- and nanoscale roughness. The wetting behavior, dependent on the concentration of cyclic tetramethyltetravinyl siloxane and hydrophobic silica nanoparticles, can be varied over a broad range to ultimately provide coatings with high static water contact angles, low contact angle hysteresis, and low roll off angles. Additionally, the cross-linked thiol-ene films show excellent chemical and solvent resistance, and high temperature stability. We demonstrate the facile nature of the spray-deposition and UV-cure process on a variety of substrate surfaces including glass, paper, stone, and cotton fabric.

EXPERIMENTAL SECTION

Materials. All reagents were obtained at the highest purity available and used without further purification unless otherwise specified. 2,2-dimethoxy-2-phenylacetophenone (DMPA), 2,4,6,8-tetramethyl-2,4,6,8-tetravinylcyclotetrasiloxane, acetone, and tetrahydrofuran (THF) were obtained from Sigma-Aldrich. Triallyl isocyanurate was obtained from TCI America. Pentaerythritol tetra(3-mercaptopropionate) was obtained from Bruno Bock. Aerosil R972, hydrophobic fumed silica with trimethylsiloxy $-Si(OCH_3)_3$ surface functionalization with an average primary particle size of 16 nm, was kindly provided by Evonik Industries.

Characterization. Static and dynamic water contact angle measurements were performed using a Ramé-Hart 200-00 Std.-Tilting B. goniometer. Static contact angles were measured using 4−6 μL water droplets. Dynamic contact angles were obtained by taking 10 measurements/s for 15 s of an advancing or receding water droplet using a syringe pump to dispense and withdraw water from the droplet on the surface at 0.150 mL/min. The roll off angle of a 6 μL drop was measured using the tilting feature of the goniometer. Image J Drop Analysis was used to analyze the droplets and determine static and dynamic contact angle values. Scanning electron microscopy (SEM) images were obtained using an FEI Quanta 200 SEM at 25 kV under high vacuum conditions. High speed video was obtained using a Phantom, version 5.1 (Vision Research, Inc., Wayne, NJ) color high speed video camera at 2100 frames per second. The videos were manipulated using Phantom 649 Camera Control software (version 9.0.649, Vision Research, Inc., Wayne, NJ). Grazing angle ATR-FTIR was conducted using a Nicolet 8700 FTIR spectrometer with a KBr beam splitter and a MCT/A detector. XPS measurements were performed using a Kratos Axis Ultra Spectrometer (Kratos Analytical, Manchester, UK) with a monochromatic Al K X-ray source (1486.6 eV) operating at 150 W under 1.0×10^{-9} Torr. Measurements were performed in hybrid mode using electrostatic and magnetic lenses, and the pass energy of the analyzer was set at 40 eV for high-resolution spectra and 160 eV for survey scans, with energy resolutions of 0.1 and 0.5 eV, respectively. Generally, total acquisition times of 180 and 440 s were used to obtain high resolution and survey spectra, respectively. For a 0° take off angle (angle between sample surface normal and the electron optical axis of the spectrometer), the maximum information depth of the measurements was approximately 8 nm.[48] All XPS spectra were recorded using the Kratos Vision II software; data files were translated to VAMAS format and processed using the CasaXPS software package (version 2.3.12). Binding energies were calibrated with respect to C 1s at 285 eV.

Film Preparation. Thiol-ene resins were prepared by weighing out thiol (PETMP), alkene (TTT/TMTVSi), and photoinitiator (DMPA) into a glass jar, maintaining a 1:1 stoichiometric ratio of thiol to alkene. A specified amount of hydrophobic silica nanoparticles (Aerosil R972 = 0, 10, 20, or 30 wt % relative to resin) was added to the resin mixture and subsequently dispersed in a low boiling organic solvent such as THF or acetone (15:1 w/w solvent/resin) by ultrasonication for 30 min. Glass slides were used as model substrates. Glass slides were cleaned via ultrasonication in ethanol and dried under a stream of nitrogen prior to use. No additional pretreatment of the glass or other surfaces was performed prior to film deposition. An air brush with a nozzle diameter of 0.635 mm (Paasch H#3 obtained from McMaster-Carr) was connected to a compressed nitrogen source (30 psi) and used to spray coat the thiol-ene resin onto the glass substrates at a distance of 20−25 cm. The coating was allowed to sit for 1 min and subsequently cured under a UV flood lamp (17 mW/cm^2) for 5 min. The films were then annealed at 40 °C for 2 h to completely remove residual solvent from the film.

RESULTS AND DISCUSSION

Film Fabrication and Composition. As shown in Figure 1, superhydrophobic coatings were fabricated from nanoparticle-laden thiol-ene resins using a simple spray coating technique with subsequent photopolymerization. The UV-curable resin, consisting of a photoinitiator, a tetrafunctional thiol (PETMP), a mixture of multifunctional enes (TTT and TMTVSi), and hydrophobic modified SiO_2 nanoparticles, was diluted with THF or acetone to reduce the viscosity and disperse the nanoparticles. The resin solution was then spray-coated onto glass substrates. The spray-coating process atomizes the resin solution and directs a random distribution of micrometer-sized droplets toward the substrate by air flow. Depending on the spray-coating parameters (i.e., nozzle size, air pressure, nozzle to substrate distance, etc.), the deposited resin may range from a fully wet layer to a "dry-sprayed" layer. In

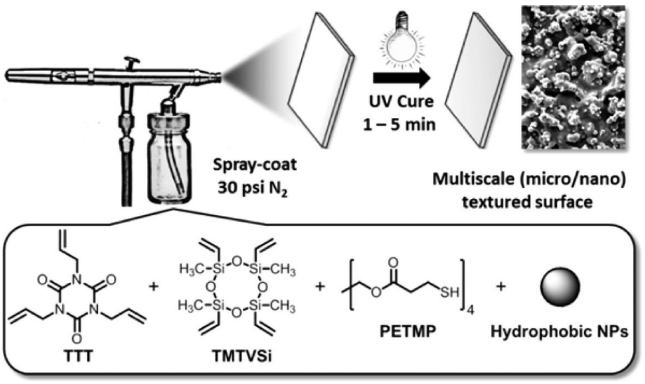

Figure 1. Schematic of the spray-deposition and photopolymerization process using hybrid inorganic–organic thiol-ene resins laden with hydrophobic silica nanoparticles.

either case, rapid solvent evaporation leads to the formation of micro- and submicrometer-sized particles rendering the surface with a porous, microstructured morphology.

Photopolymerization of the thiol-ene resin for 5 min under a UV flood lamp (17 mW/cm^2) then serves to permanently lock the obtained microstructure in place resulting in mechanically and thermally robust films. Notably, the photopolymerization was carried out under ambient conditions with no requirement of an inert atmosphere to achieve a high conversion cure – a salient feature of the chosen thiol-ene chemistry. Upon optimization of the spray-coating process, the parameters associated with the spray process were held constant as described in the Experimental Section. However, the amount of nanoparticle loading (10, 20, and 30% by weight) and the TTT:TMTVSi molar ratio (0:100, 25:75, 50:50, 75:25, and 100:0) were systematically investigated to elucidate the effects of these variables on film morphology and wetting properties of the obtained coatings. Henceforth, we will represent the various formulations as TMTVSi$_x$-TTT$_y$(z), where x and y represent the molar ratio of TMTVSi and TTT, respectively, and z represents the wt % of SiO_2. TMTVSi, a tetrafunctional siloxane monomer, was chosen to lower the surface energy and increase the hydrophobicity of the thiol-ene resin. It should be noted that, in the absence of an appropriate solvent, TMTVSi is immiscible with the TTT/PETMP base resin (vide infra). In conjunction with the spray-deposition process, the hydrophobic modified SiO_2 nanoparticles with an average primary particle size of 16 nm serve the purpose of imparting a multiscale (micro/nano), or hierarchical morphology that is necessary to achieved superhydrophobic wetting properties on the cured coatings.

The changes in film composition and extent of photopolymerization of the spray-deposited thiol-ene films were investigated using FTIR. Figure 2 shows the FTIR spectra of films containing 30 wt % SiO_2 with varying concentrations of TMTVSi. The broad peak ranging from 945 to 1285 cm^{-1} corresponds to the asymmetric Si–O–Si stretch arising from both the hydrophobic modified silica nanoparticles and cyclic siloxane ring of TMTVSi. As expected, the overall intensity of the Si–O–Si peak increases with higher molar ratios of TMTVSi. The peak at 1738 cm^{-1} is assigned to the carbonyl within PETMP, and the 1685 cm^{-1} peak is associated with the carbonyl stretch of the triazine ring of TTT. The peak at 1463 cm^{-1} is assigned to the C–N stretch within the cyclic urea structure. The intensities of the peaks at 1685 cm^{-1} and 1463

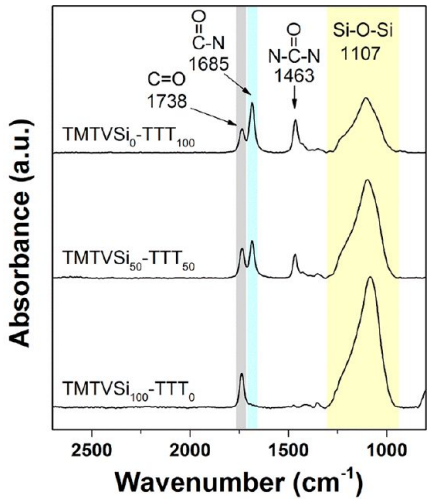

Figure 2. FTIR spectra for TMTVSi$_x$-TTT$_y$(30) containing varying concentration of TMTVSi.

cm^{-1} decrease with decreasing TTT concentration and are not observed in the TMTVSi$_{100}$-TTT$_0$(30) spectrum. Photocuring the samples under a UV flood lamp results in high conversion of both thiol (2570 cm^{-1}) and alkene functional groups in the thiol-ene polymer matrix, as little evidence for the presence of either of these groups could be observed by FTIR. For comparison, the FTIR spectra of the uncured films are provided in Supporting Information Figure S1. X-ray photoelectron spectroscopy was employed to better understand the interfacial chemical composition of the photocured samples. Si/C and Si/O ratios were calculated from the survey spectra and are shown along with the XPS survey spectra for the TMTVSi$_x$-TTT$_y$(30) sample series in Figure 3. As shown in Figure 3a, the TMTVSi$_0$-TTT$_{100}$(30) sample exhibits C1s, N1s, O1s, S2s, and Si2p peaks. The Si/C (0.767) and Si/O (0.546) ratios, as well as the attenuation of the N1s and S2s peaks, indicate the interface of TMTVSi$_0$-TTT$_{100}$(30) is composed primarily of trimethylsi-

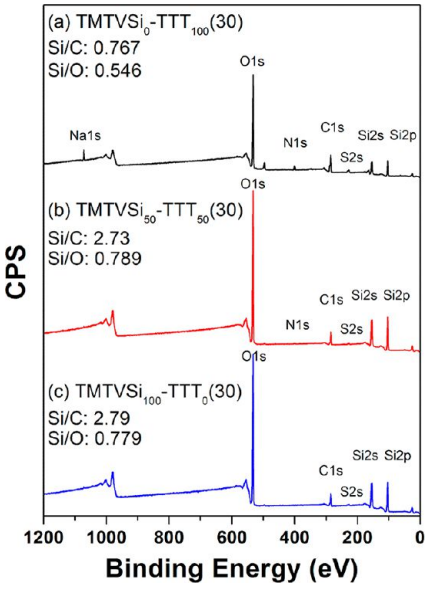

Figure 3. XPS spectra for (a) TMTVSi$_0$-TTT$_{100}$(30), (b) TMTVSi$_{50}$-TTT$_{50}$(30), and TMTVSi$_{100}$-TTT$_0$(30) films. Si/C and Si/O ratios were calculated from the respective survey spectrum for each sample.

loxy-capped silica nanoparticles with TTT-PETMP serving as a cross-linked binder to stabilize the nanoparticles at the interface. As expected, a decrease in the N1s intensity was observed for TMTVSi$_{50}$-TTT$_{50}$(30) (Figure 3b and Supporting Information Figure S2), while the N1s peak was not observed for TMTVSi$_{100}$-TTT$_0$(30) due to the absence of TTT in the formulation (Figure 3c). The Si/C and Si/O ratios for TMTVSi$_{50}$-TTT$_{50}$(30) (Si/C = 2.73; Si/O = 0.789) and TMTVSi$_{100}$-TTT$_0$(30) (Si/C = 2.73; Si/O = 0.779) were observed to be quite similar. The significant increases in the Si/C and Si/O ratios for these samples, compared with TMTVSi$_0$-TTT$_{100}$(30), indicate the interface is predominately comprised of trimethylsiloxy-capped silica nanoparticles. A Si/O ratio greater than 0.5 also indicates some degree of surface segregation of TMTVSi; however as TMTVSi and silica nanoparticles both contribute to the Si/C and Si/O ratios, we are unable to conclusively determine if the nanoparticles are resin-coated or if the nanoparticles are simply stabilized at the interface by the cross-linked resin. Undoubtedly, the predominate presence of hydrophobic silica nanoparticles at the film interface plays a significant role in the observed wetting behavior of the films (vide infra).

Surface Morphology. The surface morphologies of the cured thiol-ene films were investigated using SEM. Figure 4

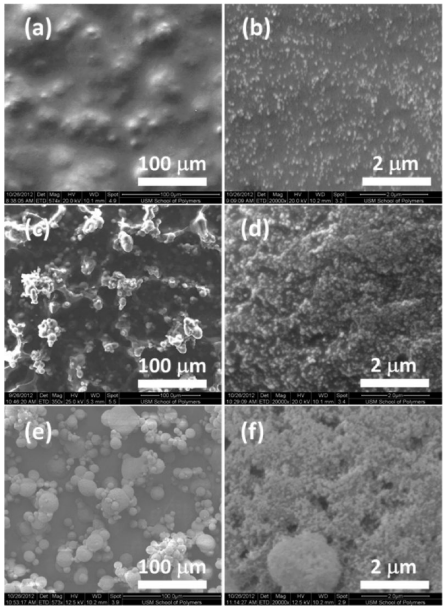

Figure 4. SEM micrographs of TMTVSi$_0$-TTT$_{100}$ with (a) 10%, (c) 20%, and (e) 30% nanoparticles with a scale of 100 μm and (b) 10%, (d) 20%, and (f) 30% nanoparticles with a scale of 2 μm.

shows the low and high magnification SEM images for the TMTVSi$_0$-TTT$_{100}$ films containing 10% (Figure 4a, b), 20% (Figure 4c, d), and 30% (Figure 4e, f) by weight SiO_2 nanoparticles. At low nanoparticle loading (Figure 4a), the surfaces exhibit a fairly smooth morphology with low porosity on the micrometer scale, and a sparse distribution of particles on the nanometer scale (Figure 4b). As the SiO_2 content is increased, the surfaces containing 20% (Figure 4c) and 30% (Figure 4e) SiO_2 exhibit an increase in surface roughness on the microscale likely derived from the combination of the spray-deposition process and nanoparticle agglomeration. Additionally, the higher magnification images show the presence of nanometer scale roughness superimposed on the larger microstructure (Figure 4d and 4f). SEM images for the TMTVSi$_{50}$-TTT$_{50}$ films containing 10%, 20%, and 30% by weight SiO_2 nanoparticles are shown in Figure 5. The

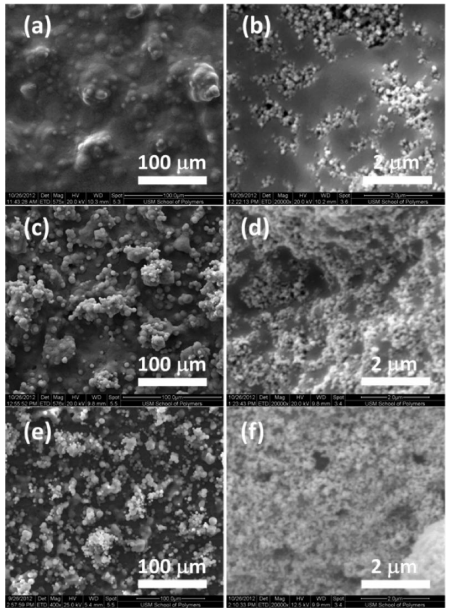

Figure 5. SEM micrographs of TMTVSi$_{50}$-TTT$_{50}$ with (a) 10%, (c) 20%, and (e) 30% nanoparticles with a scale of 100 μm and (b) 10%, (d) 20%, and (f) 30% nanoparticles with a scale of 2 μm.

morphology of the TMTVSi$_{50}$-TTT$_{50}$ films containing 10% SiO_2 generally exhibits a rough surface with low porosity on the micrometer scale (Figure 5a); however, as shown in the high magnification image (Figure 5b), nanoparticle-rich domains are randomly distributed among resin-rich domains devoid of any nanometer scale roughness. This morphology is likely due to phase separation of the TMTVSi monomer upon evaporation of the solvent, as TMTVSI is immiscible with TTT-PETMP in the absence of a suitable solvent. As the concentration of SiO_2 nanoparticles is increased to 20% (Figure 5c) and 30% (Figure 5e), the substrates are completely covered by a corpuscular layer of sphere-like microparticles that endow the surface with a highly porous microstructure. Higher magnification images of TMTVSi$_{50}$-TTT$_{50}$(20) and TMTVSi$_{50}$-TTT$_{50}$(30), shown respectively in Figure 5d and 5f, again display the presence of nanoscale features superimposed on the larger microstructure. At higher nanoparticle concentrations, phase separation of the resin is not immediately evident in the SEM images of the TMTVSi$_{50}$-TTT$_{50}$ samples. Considering the SiO_2 nanoparticles are surface modified with trimethylsiloxane functionality, the hydrophobic SiO_2 nanoparticles may play a role in compatibilizing TMTVSi with the other monomer constituents. Similar trends in morphology were observed for the TMTVSi$_{100}$-TTT$_0$ films as a function of nanoparticle loading (Supporting Information Figure S3). Overall, the presence of TMTVSi in the thiol-ene formulations containing 20% and 30% SiO_2 nanoparticles appears to provide an improved size and distribution of microstructures (i.e., compare TMTVSi$_0$-TTT$_{100}$(30) in Figure 4e with TMTVSi$_{50}$-TTT$_{50}$(30) in Figure 5e or TMTVSi$_{100}$-TTT$_0$ (30) in Supporting Information Figure S2e) on the surface leading to a higher degree of microporosity. Thus, surfaces with 20% and 30% SiO_2 exhibit the desirable hierarchical morphology comprising both micro- and nano-

meter scale roughness typically required for superhydrophobic wetting behavior.

Wetting Behavior and Durabilty. The wetting behavior of the fabricated films was evaluated by measuring the static water contact angle, dynamic contact angle, contact angle hysteresis (advancing CA minus receding CA), and roll off angle. The wetting parameters are summarized in Table 1. As shown in Table 1, the static water contact angle of the pure polymer films containing no nanoparticles increases with increasing TMTVSi concentration, an expected result as the TMTVSi is significantly more hydrophobic than TTT. Figure 6 shows the relationship between the static water contact angle and TMTVSi concentration in the thiol-ene resin for each of the SiO_2 nanoparticle loading levels. For films containing 10% SiO_2, the static CA increased steadily upon increasing the TMTVSi concentration, a trend that reflects both the transition to a more porous microstructure as previously shown from Figures 4a and 5a and Supporting Information Figure S2a, as well as an increase in the overall hydrophobicity of the thiol-ene matrix as expected with higher siloxane concentrations. At 10% SiO_2 loading, only $TMTVSi_{75}$-$TTT_{25}(10)$ and $TMTVSi_{100}$-$TTT_0(10)$ films exhibit contact angles (150.2° and 156.5°, respectively) associated with superhydrophobic wetting behavior. However, $TMTVSi_{75}$-$TTT_{25}(10)$, along with films containing <75% TMTVSi, exhibited an adhesive-type of wetting, where the water droplet was strongly pinned to the surface resulting in immeasurable dynamic CA hysteresis values and large slide angles (>90°). Such behavior is characteristic of a Wenzel wetting state in which the water droplet easily penetrates and conforms to the morphological features of these surfaces. In contrast, the $TMTVSi_{100}$-$TTT_0(10)$ film shows a low CA hysteresis (3.5°) and relatively low roll off angle (5 ± 1°) consistent with a Cassie–Baxter superhydrophobic wetting state, where the CA is greatly influenced by the surface fraction of solid versus surface fraction of air at film interface. The transition to the Cassie–Baxter wetting state is consistent with the previously described morphology, as $TMTVSi_{100}$-$TTT_0(10)$ was the first sample at 10% SiO_2 loading to exhibit the multiscale corpuscular microstructure that would result in a large ratio of liquid–air to liquid–solid contact areas required for Cassie–Baxter wetting behavior. As shown in Figure 6, the concentration of TMTVSi required to reach superhydrophobic contact angles is greatly reduced with increasing SiO_2 loading levels. Superhydrophobicity is achieved with and above the $TMTVSi_{25}$-TTT_{75} formulation with 20% SiO_2, and at all TMTVSi-TTT formulations at 30% SiO_2 loading. These series of films all exhibit low contact angle hysteresis and low roll off angles consistent with a Cassie–Baxter wetting state, a consequence of the highly porous and multiscale corpuscular morphology previously discussed. An additional indication of the Cassie–Baxter state can be observed upon submersion of the films in water (Figure 7a), where a mirror-like surface is observed because of the total internal reflection of light caused by the entrapment of air resulting in a composite liquid–vapor

Table 1. Summary of Contact Angle Data for Sprayed $TMTVSi_x$-TTT-PETMP Hybrid Inorganic–organic Thiol-ene Thin Films

SiO_2 (%)	θ_{Adv}	θ_{Static}	θ_{Rec}	θ_{Hys}	θ_{Roll}
		$TMTVSi_0$-TTT_{100}-PETMP			
0		58.6 ± 1.2			
10	67.7 ± 1.6	59.5 ± 1.7			
20	108.2 ± 2.2	100.4 ± 2.8			
30	154.8 ± 1.3	152.9 ± 1.9	150.3 ± 2.4	4.5	8 ± 2
		$TMTVSi_{25}$-TTT_{75}-PETMP			
0		69.1 ± 0.9			
10	79.4 ± 2.0	69.5 ± 3.5			
20	156.9 ± 0.7	149.7 ± 1.4	145.7 ± 0.8	11.2	8 ± 1
30	155.0 ± 1.1	153.5 ± 1.6	150.3 ± 2.4	4.7	8 ± 2
		$TMTVSi_{50}$-TTT_{50}-PETMP			
0		75.9 ± 0.9			
10	133.6 ± 1.9	124.5 ± 1.6			
20	155.9 ± 0.9	151.5 ± 2.5	150.0 ± 0.8	5.9	6 ± 1
30	156.5 ± 1.3	153.5 ± 1.3	151.5 ± 1.1	5.0	3 ± 1
		$TMTVSi_{75}$-TTT_{25}-PETMP			
0		82.1 ± 1.4			
10	157.5 ± 1.2	150.2 ± 2.6			
20	156.9 ± 0.6	153.4 ± 1.7	152.3 ± 1.3	4.6	3 ± 1
30	156.0 ± 1.5	155.7 ± 1.3	154.2 ± 1.2	1.8	2 ± 1
		$TMTVSi_{100}$-TTT_0-PETMP			
0		85.2 ± 2.9			
10	158.1 ± 1.1	156.5 ± 1.1	154.6 ± 0.8	3.5	5 ± 1
20	158.0 ± 0.7	155.2 ± 0.6	154.1 ± 0.8	3.9	5 ± 1
30	158.3 ± 1.0	155.3 ± 0.7	154.2 ± 0.8	4.1	3 ± 1

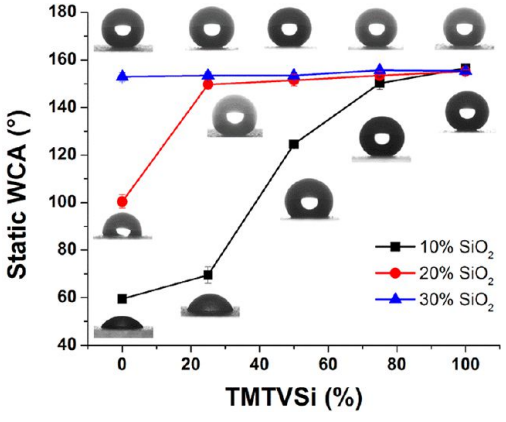

Figure 6. Variation of the static water contact angle as a function of TMTVSi concentration at 10, 20, and 30 wt % SiO_2 nanoparticle loading. Insets show the static water drop images at the respective TMTVSi concentration.

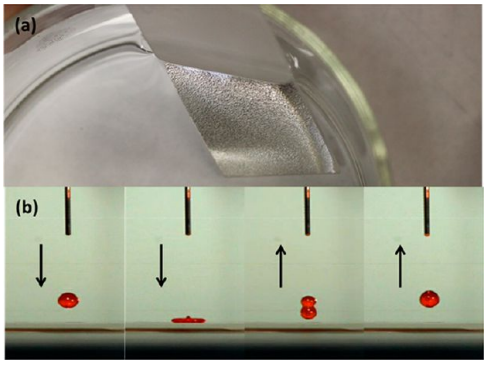

Figure 7. (a) Photograph showing the mirror-like surface resulting from the submersion of the superhydrophobic sample into water. (b) Image captures from high-speed video of a red-dyed water droplet impacting and bouncing on the $TMTVSi_{50}$-$TTT_{50}(30)$ surface. The distance from the needle to the surface is approximately 2 cm.

interface between the superhydrophobic surface and bulk water. The Cassie–Baxter wetting state was found to be stable for long submersion times and to drop impact experiments as illustrated in the series of high-speed video frame captures shown in Figure 7b. Droplets of water (dyed red for greater visibility) dropped onto the $TMTVSi_{50}$-$TTT_{50}(30)$ sample, even from distances >10 cm bounced from the surface confirming a robust Cassie–Baxter wetting state.

The stability of the cross-linked thiol-ene coatings and of the associated superhydrophobic wetting behavior was further assessed by exposure of the samples to a variety of environmental conditions. Static contact angle measurements conducted at pH 2 (aq. H_2SO_4) and pH 12 (aq. KOH) showed no observable changes in the wetting behavior of the $TMTVSi_{50}$-$TTT_{50}(30)$ samples, resulting in contact angles of 154.3° ± 0.84° and 154.4° ± 0.51°, respectively. The $TMTVSi_{50}$-$TTT_{50}(30)$ samples were exposed to 120 °C in an air circulation oven to evaluate the temperature stability of the multitextured morphology. As shown in Figure 8, the static

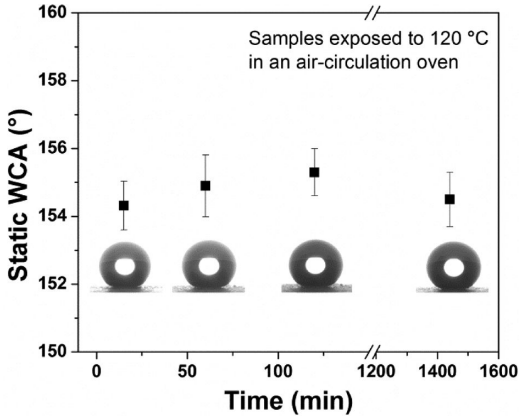

Figure 8. Static water contact angle versus exposure time at 120 °C in an air circulation oven for the $TMTVSi_{50}$-$TTT_{50}(30)$ coating.

contact angle was fairly constant over a 24 h exposure period at 120 °C illustrating the thermal stability of the microstructure, stability that can be attributed to the highly cross-linked thiol-ene polymer matrix resulting from photopolymerization. Similarly, submersion of the cured coatings in common organic solvents (acetone, toluene, etc.) resulted in no observable changes in water contact angle. Although not measured in a quantitative manner, the coatings are generally mechanically robust and are able to withstand the stresses associated with everyday handling. As shown in Supporting Information Figure S4, the static contact angle measured before (155.8°) and after (155.3°) pressing on the surface with a gloved finger remained constant in the superhydrophobic regime.

To demonstrate the versatility of this simple spray-deposition technique for the fabrication of superhydrophobic coatings, we sprayed the surface of a variety of substrates with the $TMTVSi_{50}$-$TTT_{50}(30)$ formulation and cured the coatings under a UV flood lamp. Figure 9 shows a photograph of water droplets on various treated substrates including glass, aluminum, filter paper, marble, sandstone, and cotton cloth. Water droplets on untreated regions of these substrates are also shown to illustrate the contrast in wettability. Regardless of the substrate, treatment with $TMTVSi_{50}$-$TTT_{50}(30)$ results in a stable superhydrophobic surface with high contact angles (>150°) and low roll off angles (<5°). As illustrated, the red-

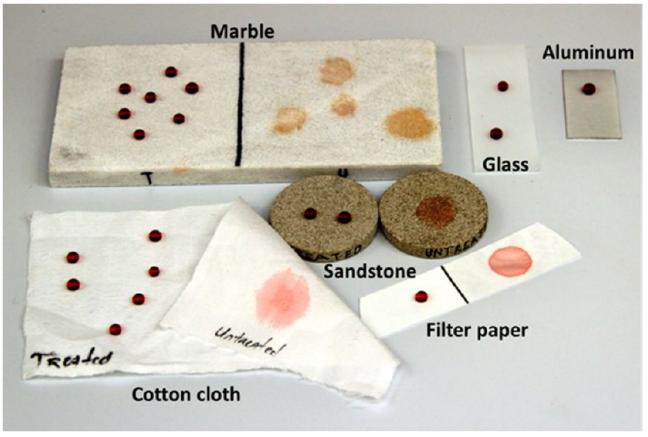

Figure 9. Photograph of various surfaces spray-coated with the $TMTVSi_{50}$-$TTT_{50}(30)$ and cured under a UV flood lamp. Shown in the photo are glass, aluminum, coated and uncoated filter paper, coated and uncoated marble and sandstone, and cotton fabric coated one side and uncoated on the reverse side.

dyed water droplets easily wet, penetrate, and stain the porous stone surfaces when untreated, but are unable to wet the stone when sprayed with $TMTVSi_{50}$-$TTT_{50}(30)$. The photo in Figure 9 also shows the ability to prepare cotton cloth with asymmetric wettability simply by spray-coating and curing only one side of the cloth. Because of the rapid evaporation of solvent during the spray-coating process, the thiol-ene resin is unable to fully penetrate through to the back side of the cotton cloth. Thus, the treated cloth shows superhydrophobic wetting on one side while retaining the original hydrophilic wetting properties of the cotton on the reverse side, as indicated by the aqueous dye wetting and ultimately staining the back side of the treated cotton fabric. We should note that our approach is not the first example of simple processing toward asymmetric wetting textiles.[49,50] For example, Liu and co-workers recently reported the fabrication of cotton fabric with single-faced superhydrophobicity using a fluoropolymer emulsion foam finishing process.[49] Nonetheless, fabrics with single-faced superhydrophobicity are of great interest in textile engineering for medical and industrial applications, including fabrics for improved performance sports and military clothing, bandages, microfluidic systems, and oil/water separations.

CONCLUSIONS

We have demonstrated a simple spray-deposition technique that enables fabrication of UV-cured, superhydrophobic coatings prepared from hybrid organic–inorganic thiol-ene precursors. The combination of the spray-deposition process and the use of hydrophobic silica nanoparticles endow the surface with a randomly dispersed corpuscular morphology exhibiting both micro- and nanometer-scale roughness as shown by SEM. With sufficient nanoparticle loading, the hierarchically structured surfaces result in high water contact angles (>150°), low contact angle hysteresis (<5°), and low roll off angles (2–5°) – all characteristics of a Cassie–Baxter wetting state. Moreover, the cross-linked thiol-ene coatings are solvent resistant, stable at low and high pH, and maintain superhydrophobic wetting behavior at elevated temperatures. The spray-deposition and UV-cure thiol-ene process was applied to various substrate materials including glass, stone, paper, metal, and fabric – all resulting in superhydrophobic surfaces. Considering the demonstrated simplicity and

versatility of the present approach, we believe the process may be scalable for treatment of large-area substrates and has potential to provide an economical route to superhydrophobic surfaces for textiles and other industrial applications.

■ ASSOCIATED CONTENT

Supporting Information

Additional FTIR, SEM, and photos illustrating mechanical stability and translucent optical properties. This material is available free of charge via the Internet at http://pubs.acs.org.

■ AUTHOR INFORMATION

Corresponding Author

*E-mail: derek.patton@usm.edu.

Author Contributions

The manuscript was written through contributions of all authors. All authors have given approval to the final version of the manuscript.

Notes

The authors declare no competing financial interest.

■ ACKNOWLEDGMENTS

The authors gratefully acknowledge financial support from the National Science Foundation (NSF SCIART DMR-1041853 and NSF CAREER DMR-1056817). B. S. thanks the US Dept. of Education GAANN Fellowship Program (Award P200A090066) for financial support. We thank Dr. Christopher M. Stafford at the National Institute of Standards and Technology (Gaithersburg) for help with XPS.

■ REFERENCES

(1) Li, X. M.; Reinhoudt, D.; Crego-Calama, M. *Chem. Soc. Rev.* **2007**, *36*, 1350−1368.
(2) Zhang, X.; Shi, F.; Niu, J.; Jiang, Y. G.; Wang, Z. Q. *J. Mater. Chem.* **2008**, *18*, 621−633.
(3) Onda, T.; Shibuichi, S.; Satoh, N.; Tsujii, K. *Langmuir* **1996**, *12*, 2125−2127.
(4) Wenzel, R. N. *Ind. Eng. Chem.* **1936**, *28*, 988−994.
(5) Cassie, A. B. D.; Baxter, S. *Trans. Faraday Soc.* **1944**, *40*, 546−551.
(6) Barthlott, W.; Neinhuis, C. *Planta* **1997**, *202*, 1−8.
(7) Hosono, E.; Fujihara, S.; Honma, I.; Zhou, H. S. *J. Am. Chem. Soc.* **2005**, *127*, 13458−13459.
(8) Shiu, J. Y.; Kuo, C. W.; Chen, P. L.; Mou, C. Y. *Chem. Mater.* **2004**, *16*, 561−564.
(9) Ahuja, A.; Taylor, J. A.; Lifton, V.; Sidorenko, A. A.; Salamon, T. R.; Lobaton, E. J.; Kolodner, P.; Krupenkin, T. N. *Langmuir* **2008**, *24*, 9−14.
(10) Zhang, G.; Wang, D. Y.; Gu, Z. Z.; Mohwald, H. *Langmuir* **2005**, *21*, 9143−9148.
(11) Ma, M.; Hill, R. M.; Lowery, J. L.; Fridrikh, S. V.; Rutledge, G. C. *Langmuir* **2005**, *21*, 5549−5554.
(12) Han, D. W.; Steckl, A. J. *Langmuir* **2009**, *25*, 9454−9462.
(13) Singh, A.; Steely, L.; Allcock, H. R. *Langmuir* **2005**, *21*, 11604−11607.
(14) Wu, J.; Wang, N.; Wang, L.; Dong, H.; Zhao, Y.; Jiang, L. *ACS Appl. Mater. Interfaces* **2012**, *4*, 3207−3212.
(15) Yoo, Y.; You, J. B.; Choi, W.; Im, S. G. *Polym. Chem.* **2013**, *4*, 1664−1671.
(16) Zhang, J.; Seeger, S. *Adv. Funct. Mater.* **2011**, *21*, 4699−4704.
(17) Pan, J.; Song, X.; Zhang, J.; Shen, H.; Xiong, Q. *J. Phys. Chem. C* **2011**, *115*, 22225−22231.
(18) Crick, C. R.; Parkin, I. P. *J. Mater. Chem.* **2011**, *21*, 14712−14716.
(19) Balu, B.; Breedveld, V.; Hess, D. W. *Langmuir* **2008**, *24*, 4785−4790.
(20) Li, L.; Breedveld, V.; Hess, D. W. *ACS Appl. Mater. Interfaces* **2012**, *4*, 4549−4556.
(21) Shirtcliffe, N. J.; McHale, G.; Newton, M. I.; Perry, C. C. *Langmuir* **2003**, *19*, 5626−5631.
(22) Tadanaga, K.; Morinaga, J.; Matsuda, A.; Minami, T. *Chem. Mater.* **2000**, *12*, 590.
(23) Kamegawa, T.; Shimizu, Y.; Yamashita, H. *Adv. Mater.* **2012**, *24*, 3697−3700.
(24) Roach, P.; Shirtcliffe, N. J.; Newton, M. I. *Soft Matter* **2008**, *4*, 224−240.
(25) Shirtcliffe, N. J.; McHale, G.; I. Newton, M. *J. Polym. Sci., Part B: Polym. Phys.* **2011**, *49*, 1203−1217.
(26) Ogihara, H.; Okagaki, J.; Saji, T. *Langmuir* **2011**, *27*, 9069−9072.
(27) Ogihara, H.; Xie, J.; Okagaki, J.; Saji, T. *Langmuir* **2012**, *28*, 4605−4608.
(28) Steele, A.; Bayer, I.; Loth, E. *Nano Lett.* **2008**, *9*, 501−505.
(29) Srinivasan, S.; Chhatre, S. S.; Mabry, J. M.; Cohen, R. E.; McKinley, G. H. *Polymer* **2011**, *52*, 3209−3218.
(30) Men, X.; Zhang, Z.; Yang, J.; Zhu, X.; Wang, K.; Jiang, W. *New J. Chem.* **2011**, *35*, 881−886.
(31) Campos, R.; Guenthner, A. J.; Meuler, A. J.; Tuteja, A.; Cohen, R. E.; McKinley, G. H.; Haddad, T. S.; Mabry, J. M. *Langmuir* **2012**, *28*, 9834−9841.
(32) Raza, A.; Si, Y.; Wang, X.; Ren, T.; Ding, B.; Yu, J.; S. Al-Theyab, S. *RSC Adv.* **2012**, *2*, 12804−12811.
(33) Wang, X.; Hu, H.; Ye, Q.; Gao, T.; Zhou, F.; Xue, Q. *J. Mater. Chem.* **2012**, *22*, 9624−9631.
(34) Mahadik, S.; Mahadik, D. B.; Kavale, M. S.; Parale, V. G.; Wagh, P. B.; Barshilia, H.; Gupta, S.; Hegde, N. D.; Rao, A. V. *J. Sol−Gel Sci. Technol.* **2012**, *63*, 580−586.
(35) Hwang, H. S.; Kim, N. H.; Lee, S. G.; Lee, D. Y.; Cho, K.; Park, I. *ACS Appl. Mater. Interfaces* **2011**, *3*, 2179−2183.
(36) Guo, Y.; Tang, D.; Gong, Z. *J. Phys. Chem. C* **2012**, *116*, 26284−26294.
(37) Simsek, E.; Acatay, K.; Menceloglu, Y. Z. *Langmuir* **2012**, *28*, 14192−14201.
(38) Steele, A.; Bayer, I.; Loth, E. *J. Appl. Polym. Sci.* **2012**, *125*, E445−E452.
(39) Verho, T.; Bower, C.; Andrew, P.; Franssila, S.; Ikkala, O.; Ras, R. H. A. *Adv. Mater.* **2011**, *23*, 673−678.
(40) Jin, H.; Tian, X.; Ikkala, O.; Ras, R. H. A. *ACS Appl. Mater. Interfaces* **2013**, *5*, 485−488.
(41) Jung, Y. C.; Bhushan, B. *ACS Nano* **2009**, *3*, 4155−4163.
(42) Su, C.; Xu, Y.; Gong, F.; Wang, F.; Li, C. *Soft Matter* **2010**, *6*, 6068−6071.
(43) Tiwari, M. K.; Bayer, I. S.; Jursich, G. M.; Schutzius, T. M.; Megaridis, C. M. *ACS Appl. Mater. Interfaces* **2010**, *2*, 1114−1119.
(44) Bayer, I. S.; Fragouli, D.; Martorana, P. J.; Martiradonna, L.; Cingolani, R.; Athanassiou, A. *Soft Matter* **2011**, *7*, 7939−7943.
(45) Schwalm, R. *UV Coatings: Basics, Recent Developments and New Applications*; Elsevier: Amsterdam, 2007.
(46) Hoyle, C. E.; Bowman, C. N. *Angew. Chem., Int. Ed.* **2010**, *49*, 1540−1573.
(47) Hoyle, C. E.; Lee, T. Y.; Roper, T. *J. Polym. Sci., Part A: Polym. Chem.* **2004**, *42*, 5301−5338.
(48) Seah, M. P.; Dench, W. A. *Surf. Interface Anal.* **1979**, *1*, 2−11.
(49) Liu, Y.; Xin, J. H.; Choi, C.-H. *Langmuir* **2012**, *28*, 17426−17434.
(50) Wang, H.; Ding, J.; Dai, L.; Wang, X.; Lin, T. *J. Mater. Chem.* **2010**, *20*, 7938−7940.